A reliable new potential energy surface for H_2–Ar

Carey Bissonnette, Claudio E. Chuaqui,[a] Kenneth G. Crowell, and Robert J. Le Roy
Guelph–Waterloo Center for Graduate Work in Chemistry, University of Waterloo, Waterloo, Ontario N2L 3G1, Canada

Richard J. Wheatley[b] and William J. Meath[c]
Department of Chemistry, University of Western Ontario, London, Ontario N6A 3B7, Canada

(Received 17 January 1996; accepted 6 May 1996)

A reliable new three-dimensional potential energy surface is obtained for the H_2–Ar system using an exchange-coulomb potential model with five parameters determined empirically from a least-squares fit to experimental data. This surface fully accounts for new high resolution IR data, virial coefficients, and vibrational transition pressure-shifting coefficients used in the analysis, and yields excellent predictions of elastic and inelastic scattering cross sections and hyperfine transition intensities not included in the analysis. Quantitative comparisons with the best previous empirical potential and a high quality fully *ab initio* potential are also presented. © *1996 American Institute of Physics.* [S0021-9606(96)00331-5]

I. INTRODUCTION

This paper has two main objectives. One of these is to exploit McKellar's new high resolution discrete infrared spectra[1] for H_2–Ar and D_2–Ar to obtain a reliable new potential energy surface for these species, which accurately explains a wide variety of experimental data and has good predictive ability. The other is the more general objective of developing and testing an improved model for representing multidimensional atom–molecule and molecule–molecule potential energy surfaces. In the latter regard, attention is focussed on the exchange-coulomb (XC) model[2–4] which was originally developed for describing the interactions of closed shell atoms, and has been shown to yield potential energy curves for rare gas systems that reliably predict a wide variety of properties.[5] More recently the model has been modified to forms appropriate for interactions involving molecules,[6–9] and has been used to obtain high quality two-dimensional potential energy surfaces for He–CO, Kr–N_2, and Ar–N_2.[10–12] An objective of this paper is to test the utility of the XC model for representing full three-dimensional atom–diatom potential energy surfaces. To this end, it is used in a fit to the new higher resolution discrete IR spectra for isotopic H_2–Ar, seeking to obtain an improved potential energy surface for this system.

The first ever quantitative determination of full three-dimensional atom–diatom potential energy surfaces from experimental data, reported in 1974,[13] was based on an analysis of the fully resolved portion of McKellar and Welsh's discrete IR spectra for the H_2–Rg (Rg=Ar, Kr, and Xe) systems.[14] Since that time, improved empirical surfaces for those systems, based on both better data and more realistic radial potential forms, have been published.[15–18] Impressive developments in experimental methodology over the past decade and a half have led to the measurement of exquisite high resolution spectroscopic data for a wide variety of other atom–molecule and molecule–molecule systems. However, quantitative analyses of those data to obtain detailed potential energy surfaces have only been reported for a handful of species, and the H_2–Rg systems are still the only ones for which these surfaces explicitly incorporate the dependence on the intramolecular bond coordinates. For example, while Hutson has determined detailed potential energy surfaces for Ar–HCl and Ar–HF which accurately accounted for all of the available microwave and IR spectra for all common isotopomers, the dependence of these surfaces on the diatom bond lengths was treated approximately.[19,20] Similarly, while the pioneering three- and four-dimensional surfaces for Ar–H_2O, Ar–NH_3, and $(HCl)_2$ determined by the Saykally group depend on all van der Waals degrees of freedom,[21–23] the molecules forming these complexes are treated as essentially rigid.

The reasons for this situation are twofold. Until the current decade, limits to both computers and computational methods made iterative accurate modeling of experimental data for complexes formed from strongly anisotropic or non-hydride molecules prohibitively expensive. This restriction is now being lifted,[24–30] and an underlying problem is becoming increasingly evident as more complicated systems are studied. It is associated with devising functional forms able to accurately model a multidimensional potential energy surface using only a modest number of empirical parameters. In the earliest quantitative multidimensional analyses of atom–diatom systems, potentials were expressed as a nested sum of a power series in the diatom stretching coordinate $\xi=(r-r_0)/r_0$ with a Legendre series for the relative orientation dependence,

$$V(R,r,\theta)=\sum_{\lambda=0}\sum_{k=0}\xi^k P_\lambda(\cos\theta)V_{\lambda,k}(R), \tag{1}$$

where R is the distance from the diatom center of mass to the

[a]Present address: Department of Chemistry, University of British Columbia, 2036 Main Mall, Vancouver, BC V6T 1Z1, Canada.
[b]Present address: Department of Chemistry, University of Nottingham, Nottingham NG7 2RD, UK.
[c]Associated with the Centre for Interdisciplinary Studies in Chemical Physics, University of Western Ontario, London, Ontario N6A 3B7, Canada.

atom, θ the orientation of the diatom relative to the axis R of the complex, r the diatom bond length, and r_0 a reference length. However, while general and flexible, the expansion of Eq. (1) typically requires at least two empirical parameters for each radial strength function $V_{\lambda,k}(R)$, and without the introduction of external constraints, even for the relatively simple H_2–Rg systems the number of parameters required to define the surface threatened to become excessive.[13,18]

For complexes more strongly anisotropic than those formed from H_2, empirical potentials based on independent parametrization of the $V_{\lambda,k}(R)$ functions of the double expansion of Eq. (1) become impractical, as the numbers of variable parameters required to define the potential properly would outstrip the information content of the data long before a reliable potential was obtained. A first step in addressing this difficulty has been the adoption of Pack's approach[31] of replacing the linear Legendre potential expansion of Eq. (1) by linear Legendre expansions in the anisotropy of parameters defining the radial behavior of the potential. This was tested for the H_2–Rg systems[18] and successfully used to define the recommended fitted surfaces for Ar–HF, Ar–HCl, Ar–H_2O, and Ar–NH_3.[19–22] However, even with the induction and dispersion coefficients defining the attractive part of the potential held fixed at theoretical values, this approach still required the introduction of a substantial number of empirical parameters (21 or 22 for the Ar–HX systems and 12 or 13 for the others), and the associated difficulties would be greatly compounded if one attempted to take account of monomer vibrational stretching in the same way.

Hutson considered the latter problem when selecting a means of representing the diatom-stretching (ξ) dependence of the Ar–HF and Ar–HCl potentials. He decided that in view of possible ambiguities regarding the relative importance of linear, quadratic, and higher-order terms, the simplest solution was to approximate the bond-length dependence by an effective dependence on the mass-reduced vibrational quantum number.[19,20] The resulting surfaces accurately explain spectroscopic transition frequencies and other system properties which are essentially ''diagonal'' in the diatom vibrational state index. However, the absence of explicit bond-length dependence means that they cannot yield predictions of ''off-diagonal'' properties such as vibrational predissociation rates and vibrationally inelastic collision cross sections, or take account of centrifugal stretching of the diatom monomer.

In other work it has been shown that even the effective two-dimensional (R- and θ-dependent) potential determined from accurate fits to high resolution data for a system as simple as He–CO can have substantial model dependence.[10,32–34] Moreover, the problem of devising appropriately sophisticated potential forms which do not require an excessive number of empirical parameters to define them will clearly become increasingly severe when the component atom and/or diatom monomers are replaced by more complex species. The present approach to this problem is to express the potential in terms of theoretically based functions which incorporate the shapes of the component molecules and can be conveniently scaled to optimize the overall agreement with experiment. The experience gained here should facilitate the extension of this approach to more complicated atom–molecule and molecule–molecule systems.

There are a number of recent approaches for constructing potential energy surfaces for interactions involving closed shell species that are based on energy components which are available from relatively inexpensive *ab initio* calculations. These models[2–6,10–12,35–39] can realistically represent the most important features of the interaction, including effects due to the internal bond-length dependence of the individual monomers. All of these methods employ the best available long-range multipolar interaction energies, corrected for the neglect of charge overlap effects through the use of multiplicative damping and corrector functions, to model the main attractive part of the interaction energy. While the other approaches use supermolecule self-consistent field (SCF) dimer interaction energies to represent the mostly repulsive part of the interaction energy, the XC model employs the Heitler–London interaction energy (the sum of the first-order Coulomb and exchange energies) for this purpose. Since the latter calculation only requires the SCF wave functions for the interacting monomers, the XC model is the easiest to apply. This model also incorporates a modest number of scaling parameters whose introduction has been found to be necessary to obtain high quality potential energy surfaces for both (rare gas)–(rare gas) and two-dimensional (rare gas)–molecule interactions.[5,10–12] In passing, we remark that in the hands of Aziz and co-workers,[5,40,41] the analogous flexibility inherent in the Hartree–Fock-dispersion (HFD) potential energy model[35] has been used to determine high quality (rare gas)–(rare gas) potentials.

In this paper, the XC model is used to obtain a full three-dimensional state-of-the-art potential energy surface for the prototype atom–diatom system, H_2–Ar. The adjustable parameters in the model are determined by fitting to the improved and extended IR data of McKellar,[1] to pressure shifting coefficients for the Raman transitions of H_2 in Ar measured by Farrow *et al.*[42] and Berger *et al.*,[43] and to the second virial coefficients of Brewer and Vaughn[44] and Schramm and co-workers.[45] H_2–Ar has been one of the most extensively studied atom–diatom systems; a wide variety of high quality experimental data has been collected and has been used in determining and/or testing various potential energy surfaces. Moreover, the best empirical surface[18] for H_2–Ar, known as the TT_3 potential, has been used as a reference against which *ab initio* methods for calculating van der Waals interaction potentials can be tested.[46] On the other hand, tests against some data which were not used in its determination show that the TT_3 potential has some deficiencies. In particular, the proton spin–lattice relaxation measurements of Lemaire *et al.*[47] suggest that there are some problems with its short-range anisotropy. In addition, Green found[48] that pressure shifting coefficients for the $Q_1(J)$ Raman lines predicted from this potential surface were in very substantial disagreement with experiment, a problem which has been attributed to deficiencies in the ξ dependence of its short-range repulsive wall.[48,49] Together with the fact

that greatly improved spectroscopic data have become available for this system,[1] this motivated our choice of H_2–Ar as a system for testing the utility of the XC model for determining a full three-dimensional atom–diatom potential energy surface.

The three-dimensional XC potential model for H_2–Ar is described in Sec. II. The experimental data used to help construct the final potential energy surface, and the methods used to simulate and fit to the data, are discussed in detail in Secs. III and IV. The optimized XC potential energy surface for H_2–Ar is then presented and compared with other potentials reported in the literature in Secs. V–VII, while a brief summary of the more important features of this work is contained in Sec. VIII.

II. THE EXCHANGE-COULOMB MODEL POTENTIAL FOR H_2–Ar

The Jacobi coordinates $\mathbf{r}=r\hat{\mathbf{r}}$, $\mathbf{R}=R\hat{\mathbf{R}}$, and θ are convenient for describing the dynamics of the H_2–Ar system, since the potential energy depends only on the scalar quantities R, r, and θ. Here, $\hat{\mathbf{r}}$ is a unit vector directed along the axis of the diatom of bond length r, and $\hat{\mathbf{R}}$ is a unit vector which is directed from the center of mass of the diatom to the Ar atom, which lies a distance R from the H_2 center of mass. The angle between these two units vectors is $\theta=\cos^{-1}(\hat{\mathbf{r}}\cdot\hat{\mathbf{R}})$.

In the variant of the XC model[2–4,6] used here, which is a diatom bond-length-dependent extension of the two-dimensional XC potential energy models used previously,[10–12] the intermolecular potential is written as

$$V(R,\theta,\xi)=FE_{\mathrm{HL}}^{(1)}(R,\theta,\xi)+\Delta E_C(R,\theta,\xi)$$
$$=FE_{\mathrm{HL}}^{(1)}(R,\theta,\xi)-G_{10}(R,\theta)$$
$$\times\sum_{n=6(2)}^{10} f_n(R,\theta)C_n(\theta,\xi)R^{-n}, \qquad (2)$$

where $\xi\equiv(r-r_0)/r_0$, and $r_0=1.448\,739a_0$ is the expectation value of r for H_2 in its ground rovibrational level.[50] The quantity F is an empirical function which will be discussed in more detail below, $E_{\mathrm{HL}}^{(1)}$ is the first-order Heitler–London energy, and ΔE_C, the main attractive part of the potential energy model, is an individually damped, overall-corrected, dispersion plus induction energy series representing the second- and higher-order Coulomb interaction energy. The individual damping functions f_n take account of nonnegligible charge overlap effects neglected in the R^{-n} multipolar expansion of the second-order Coulomb interaction energy, and prevent these inverse-power terms from diverging at small R.[4,6,51,52] The overall corrector function G_{10} represents the effect of other higher-order terms not explicitly included in the potential model.[4,6]

The Heitler–London interaction energy $E_{\mathrm{HL}}^{(1)}$ was evaluated using the CADPAC program,[53] including the Hayes–Stone perturbation theory program.[54] The calculations are analogous to those reported earlier for a fixed H_2 bond length of $r=1.4a_0$,[7] and are based on high quality SCF wave functions for the isolated monomers.[55] Heitler–London energies were obtained at seven equally spaced values of $R(3a_0\leqslant R\leqslant 9a_0)$, four values of θ, and five H_2 bond lengths $(1.1a_0\leqslant r\leqslant 1.9a_0)$. These computed energies were fit to the form

$$E_{\mathrm{HL}}^{(1)}(R,\theta,\xi)=K\ \exp[-(R-R_s)(b_0+b_1z+b_2z^2)]$$
$$\times\sum_{\lambda=0(2)}^{6}\sum_{k=0}^{3}\sum_{p=0}^{3} a_{p,k}^{(\lambda)}z^p\xi^kP_\lambda(\cos\ \theta), \qquad (3)$$

where $P_\lambda(\cos\theta)$ is a Legendre polynomial, $z\equiv(R-R_s)/(R+R_s)$, and $a_{0,0}^{(0)}=1$. Note too (see Table I) that many of the $a_{p,k}^{(\lambda)}$ expansion parameters allowed by these summation limits turn out to be statistically insignificant, and are not required to give an accurate fit.

The reference distance R_s appearing in Eq. (3) can be chosen in many ways, but a particularly accurate and economical (in terms of the number of parameters) representation of $E_{\mathrm{HL}}^{(1)}$ is obtained if R_s is set equal to the angle-dependent position of the radial potential minimum for the momomer stretching coordinate fixed at $\xi=0$:

$$R_s=R_m(\theta,\xi=0)=\sum_{\lambda=0(2)}^{4} R_m^{(\lambda)}P_\lambda(\cos\ \theta). \qquad (4)$$

In practice, an initial representation of $E_{\mathrm{HL}}^{(1)}$ is obtained using some reasonable fixed R_s value (e.g., $R_s=6.8a_0$), and the resulting $E_{\mathrm{HL}}^{(1)}$ function combined with ΔE_C to yield an overall potential from which the actual $R_m(\theta,\xi=0)$ function may be determined. Iteratively repeating the fit to the $E_{\mathrm{HL}}^{(1)}$ data with R_s set at successively refined representations of $R_m(\theta,\xi=0)$ yields rapid convergence to the desired self-consistent form. This approach yields a very precise representation of the *ab initio* points, its root mean square deviation being less than 0.1%; the resulting constants K, b_i, $a_{pk}^{(\lambda)}$, and $R_m^{(\lambda)}$ defining this $E_{\mathrm{HL}}^{(1)}$ function are listed in Table I.[56] The Heitler–London term is clearly basically repulsive, decaying exponentially with increasing R. Note that our par-

TABLE I. Dimensionless parameters $\{a_{p,k}^{(\lambda)}\}$ defining our fit of Eq. (3) to the Heitler–London energies for the XC potential of H_2–Ar. Other parameters involved in the fit are: $K=257.9888\times10^{-6}E_h$, $b_0=1.892\,368a_0^{-1}$, $b_1=0.306\,504a_0^{-1}$, $b_2=0.125\,22a_0^{-1}$, while the scaling distance expansion parameters of Eq. (4) are: $R_m^{(0)}=6.783\,754a_0$, $R_m^{(2)}=0.041\,267a_0$, and $R_m^{(4)}=-0.002\,328a_0$.

λ	p	$k=0$	$k=1$	$k=2$	$k=3$
0	0	1.0	1.438 59	0.757 37	0.0794
0	1	0.0	3.811 75	5.146 5	1.7411
0	2	0.0	3.680 8	11.684 6	7.334
0	3	0.0	2.731 4	9.880	8.451
2	0	0.160 895	0.677 00	0.943 95	0.6064
2	1	−0.092 55	0.380 5	2.360 4	3.350
2	2	0.291 51	0.864 6	3.895	5.513
2	3	0.0	0.0	3.483	0.0
4	0	0.009 315	0.043 09	0.117 96	0.1509
4	1	−0.008 52	0.0	0.104 4	0.0
4	2	0.043 11	0.198 4	0.0	0.0
4	3	−0.115 5	−0.585 5	−1.911	0.0
6	0	0.000 739	0.003 97	0.0	0.0
6	1	0.0	0.0	0.0	0.0
6	2	0.0	0.0	0.0	0.0
6	3	0.0	−0.132	−1.065	0.0

TABLE II. Values of the $\{A_n\}$, $\{B_n\}$, and $\{D_n\}$ constants characterizing the damping functions $f_n(R,\theta)$ of Eq. (5), in atomic units (Ref. 52).

	$n=6$	8	10
A_n	0.364 8	0.307 3	0.251 4
B_n	0.033 60	0.024 69	0.023 79
D_n	0.001 651	0.001 227	0.000 566 4

ticular definition of R_s affects the analytic *representation* of $E_{\rm HL}^{(1)}$ but it should have negligible effects on the resulting potential function.

The multipolar representation of the long-range interaction energy used in ΔE_C in Eq. (2), is based on the best available values of the coefficients $C_n(\theta,\xi)$,[57,58] but a key feature of the XC model is the corrector and damping functions, G_{10} and f_n, which appear in the second term of Eq. (2). They are not calculated directly for the interaction of interest, but rather are estimated by scaling the analogous functions for the nonbonded $H_2(^3\Sigma_u^+)$ interaction, which are known essentially exactly:[4,52]

$$f_n(R,\theta)=[1-\exp(-A_nSR-B_n(SR)^2-D_n(SR)^3)]^n,$$
$$G_{10}(R,\theta)=1+41.34\,\exp(-0.858\,8SR). \tag{5}$$

The constants A_n, B_n, and D_n are known for the $H_2(^3\Sigma_u^+)$ interaction (for which $S\equiv 1$),[52] and are listed in Table II. The scaling factor S depends on the relative sizes of $H_2(^3\Sigma_u^+)$ and H_2–Ar, and is used to map the functions derived for the H–H interaction onto the range of the H_2–Ar potential. The recommended[6,10–12] definition of S is one which introduces anisotropy into the damping and corrector functions, $S=R_m^{\rm H-H}/R_m(\theta,\xi=0)$, where $R_m^{\rm H-H}=7.82a_0$ is the position of the minimum for the $H_2(^3\Sigma_u^+)$ interaction and $R_m(\theta,\xi=0)$ is as defined above. As outlined above, the values of $R_m(\theta,\xi=0)$, and hence of S, are determined iteratively once the rest of the potential is specified; for more details see Refs. 2–6, 10–12, and 33. While $R_m(\theta)$ (and hence S) could also be expressed as a function of ξ, that would introduce considerable complications into the potential model, and since the effects on the potential energy surface are expected to be modest, they can be implicitly incorporated in other parts of the model. Note that in contrast to the situation for the representation of $E_{\rm HL}^{(1)}$, the values of $R_m(\theta)$ *do* affect the values of the resulting potential function.

The long-range multipole interaction coefficients $C_n(\theta,\xi)$ appearing in Eq. (2), which in general contain both dispersion and induction contributions, are expanded as

$$C_n(\theta,\xi)=\sum_{\lambda=0}^{n-4} C_n^{(\lambda)}(\xi)P_\lambda(\cos\,\theta)$$
$$=\sum_{\lambda=0(2)}^{n-4}\sum_{k=0}^{4} C_n^{\lambda,k}\,P_\lambda(\cos\,\theta)\xi^k, \tag{6}$$

where $C_n^{(\lambda)}(\xi)=0$ when λ is odd. The fact that the H_2–Ar potential energy surface collapses to the one-dimensional He–Ar potential curve when $\xi\to-1$ also means that $C_n^{(\lambda)}(\xi=-1)=0$ when $\lambda>0$. For fixed values of n and λ, the latter condition can be used to constrain the value of one of the expansion coefficients, since

$$C_n^{\lambda,4}=-\sum_{k=0}^{3}(-1)^k C_n^{\lambda,k} \quad \text{for } \lambda>0. \tag{7}$$

Anisotropic dispersion and induction coefficients $C_n^{(\lambda)}(\xi)$ for a number of (rare gas)–H_2 interactions have been computed by Wormer *et al.*[57] The dispersion coefficients were calculated from dynamic multipole polarizabilities of H_2 and of the rare gas atoms, while the induction coefficients were derived from the multipole moments of H_2 and the static polarizabilities of the atoms. These *ab initio* results for the vibrationally averaged (over ξ) $C_6^{(0)}$ and $C_6^{(2)}$ values are, respectively, only 0.5% and 1.5% lower than the accurate values determined by constrained dipole oscillator strength (DOSD) techniques.[58]

The total calculated long-range coefficients $C_n^{(\lambda)}(\xi)$ are listed in Table III, together with their estimated uncertainties; the *ab initio* results for $C_6^{(0)}$ and $C_6^{(2)}$ were scaled to reproduce the DOSD values.[58] For $n>6$ these $C_n^{(\lambda)}$ values contain both dispersion and induction contributions, and we have assumed in Eq. (2) that the induction energy damping functions are the same as those for the corresponding dispersion terms. This is not unreasonable, since the attractive part of

TABLE III. *Ab initio* values of composite dispersion and induction coefficients $C_n^{(\lambda)}(\xi)$ for H_2–Ar, in atomic units (Ref. 57). The values of $C_6^{(0)}$ and $C_6^{(2)}$ were scaled to reproduce the accurately known values obtained from dipole oscillator strength distributions (Ref. 58).

r/a_0	ξ[a]	$C_6^{(0)}$	$C_6^{(2)}$	$C_8^{(0)}$	$C_8^{(2)}$	$C_8^{(4)}$	$C_{10}^{(0)}$	$C_{10}^{(2)}$	$C_{10}^{(4)}$	$C_{10}^{(6)}$
0.0	−1.0	9.502[b]	0	157[b]	0	0	3 605[b]	0	0	0
1.0	−0.310	20.419	1.159	409.25	48.478	1.489	10 128	1 338	39	8.2
1.2	−0.172	23.560	1.739	488.42	81.169	3.400	12 458	2 376	124	16.9
1.4	−0.034	26.821	2.433	575.43	127.130	6.360	15 114	3 905	249	25.3
1.449	0.000	27.630	2.620	597.81	140.670	7.280	15 811	4 366	287	27.2
1.65	0.139	30.952	3.435	693.41	206.720	11.930	18 845	6 660	500	39.6
2.0	0.381	36.545	4.972	871.01	367.400	23.970	24 766	12 538	1206	80.3
3.0	1.071	47.150	7.8892	1378.10	1205.300	79.130	44 691	48 965	8752	477.2
Uncertainty:		±1%	±1%	±3%	±8%	±12%	±8%	±15%	±25%	±40%

[a]$\xi=(r-r_0)/r_0$, with $r_0=1.448\,739a_0$.
[b]These $r=0$ values are based on Ref. 80, with $C_6^{(0)}$ being scaled to take account of the DOSD results, and the uncertainties in $C_6^{(0)}$, $C_8^{(0)}$, and $C_{10}^{(0)}$ taken to be ±5%, ±15%, and ±30%, respectively.

the H_2–Ar interaction is dominated by the dispersion energy and little is known about induction energy damping functions for interactions involving molecules.

Part of the success of the XC potential energy model in yielding reliable (rare gas)–(rare gas) and two-dimensional (rare gas)–molecule potentials,[5,10–12] and of the HFD model in treating (rare gas)–(rare gas) potentials,[5,40,41] is due to the use of the flexibility in the model associated with the uncertainties in the input dispersion energy coefficients. This involved allowing those coefficients to vary within their estimated uncertainties when fitting to experimental data. In the present application of the XC model to H_2–Ar, we extend this idea and introduce a more general way of taking account of these uncertainties.

In most previous modeling of multidimensional van der Waals potential energy surfaces, the long-range potential energy expansion coefficients were obtained from (fits to) the best input values, and then held rigidly fixed at those values. As pointed out above, this overlooks the very real uncertainties in the calculated values of $C_n^{(\lambda)}(\xi)$, uncertainties which tend to increase rapidly with n and λ, and it introduces unnecessary rigidity into the potential model. While one could allow selected expansion coefficients $C_n^{\lambda,k}$ to vary, obtaining meaningful estimates of their individual uncertainties is quite impractical. The present approach therefore focuses on the theoretical $C_n^{(\lambda)}(\xi)$ values, for which realistic uncertainties *can* be estimated. These quantities are treated as *ab initio* ''data'' and the coefficients $C_n^{\lambda,k}$ introduced as additional parameters in our least-squares fits to optimize the model potential. This would superficially appear to involve a large increase in the number of empirical parameters required to define the XC potential energy surface. In practice, however, the $C_n^{\lambda,k}$ coefficients are largely determined by the input $C_n^{(\lambda)}(\xi)$ values and their estimated uncertainties, and for the most part are only modestly affected by the concurrent fitting to the experimental data. Therefore, the only unconstrained empirical adjustable parameters defining the XC model are those defining the scaling factor F appearing in Eq. (2).

The scaling function F is in general expected to be a weak function of R, θ, and ξ.[10–12] In the present work it proved adequate to represent it as a function of θ and ξ only,

$$F = F_{0,0} + F_{0,1}\xi + (F_{2,0} + F_{2,1}\xi)P_2(\cos\,\theta). \tag{8}$$

More sophisticated parametrizations of F were also considered, but the resulting modest improvement in the quality of fit to the experimental data did not justify the increased complexity.

In summary, the XC model potential for H_2–Ar is defined by Eqs. (2)–(8). Fixing $F=1$ and determining values of the $C_n^{\lambda,k}$ coefficients solely from a fit to the input $C_n^{\lambda}(\xi)$ coefficients given in Table III then defines a theoretical ''starting'' potential, labeled XC(0), which contains *no* empirical parameters. While realistic, this three-dimensional surface is not expected to be quantitatively accurate, and optimization of the model involves using a least-squares fit to experimental data to determine the modestly varying scaling factor $F=F(R,\theta,\xi)$ and to adjust the $C_n^{\lambda}(\xi)$ expansions. Before describing these fits, however, we will discuss the nature of the experimental data available for this system.

III. EXPERIMENTAL DATA USED IN THE ANALYSIS

One objective of this study is to use a fit to experimental data to determine a refined three-dimensional XC potential energy surface for H_2–Ar. The experimental data set used to this end consists of IR spectroscopic frequencies for H_2–Ar bimers,[1] pressure shifting coefficients for Raman transitions of H_2 in Ar,[42,43] and second virial coefficients measured for the H_2–Ar mixture.[44,45] While these types of data are complementary, the spectroscopic data is the most important source of information. However, it primarily contains information about the potential in the vicinity of the potential energy well, whereas the pressure shifting and virial data are relatively more sensitive to the H_2–Ar interaction for smaller intermolecular separations. Independent tests of the resulting surface will then be provided by comparisons with elastic and inelastic differential scattering cross sections[59,60] and with hyperfine transition measurements.[61]

The newly measured infrared spectra obtained by McKellar for H_2–Ar and D_2–Ar are described in detail in the accompanying paper.[1] In addition to its improved precision, the new data set differs from those[14,62] used in previous analyses[13,15,17,18] in three ways. First, the presence of far-IR transitions corresponding to $\Delta v(\text{diatom})=0$, in addition to mid-IR data for $\Delta v(\text{diatom})=1$, makes the analysis much more directly sensitive to the ξ dependence of the potential anisotropy. In the same vein, the observation of $\Delta v=2$ transitions effectively doubles the range of ξ directly probed by these experiments. In addition, the observation of transitions into the first vibrationally excited van der Waals stretching state ($n=1\rightarrow 0$ or $1\leftarrow 0$ transitions) greatly increases the sensitivity to the shape of the outer portion of the potential well. Thus, the new IR data set has substantial qualitative and quantitative improvements over those available previously. This clearly means that it should provide a critical test of the XC potential model, and that refining the XC(0) surface using a fit to those data should yield a potential of substantially higher quality than currently available. Note too that our analysis simultaneously fits to 94 transition frequencies for H_2–Ar and 77 for D_2–Ar, with the differences between the isotopomers being automatically accounted for by appropriate averaging over the ξ dependence of the potential energy surfaces.

The method used for calculating the transition frequencies (and predissociation line widths) is the secular equation/perturbation theory (SEPT) method of Hutson and Le Roy.[63] For the H_2–(rare gas) systems this method is extremely efficient and gives calculated energy levels and other properties which are essentially exact for a given potential energy surface. This same method was also used for calculating the hyperfine transition frequencies discussed in Sec. VII. As in all of the calculations reported here, the values of the atomic masses and physical constants were taken from Ref. 64.

The pressure shifting coefficients for the H_2–Ar system indicate how the H_2 transition frequencies are shifted by col-

lisional interactions in an Ar bath gas. These shifts are due to perturbation of the monomer level energies induced by collisions between hydrogen and argon. The experimental pressure shifting coefficients used in our analysis are those for the $Q_1(0)$ Raman line of H_2 in Ar reported by Farrow *et al.*[42] and Berger *et al.*[43] Earlier measurements reported by Lallemand and Simova[65] have been omitted from the fits, since they cover only a narrow temperature range and are effectively supplanted by the more accurate modern data.

The conventional method for calculating accurate pressure shifting coefficients is based on close-coupling (CC) scattering calculations;[48,66–68] however, they are far too demanding to be incorporated into an iterative least-squares fitting procedure. We have therefore employed an approximate, semiclassical quasistatic (QS) method for calculating the pressure shifting coefficients.[49] According to the QS model, the pressure shifting coefficient $\Delta\nu_{\rm QS}(T)$ for the $(v'',j'')\rightarrow(v',j')$ Raman transition of H_2 is

$$\Delta\nu_{\rm QS}(T)=4\pi\rho_0\int_0^\infty R^2dR[\overline{V_0^{v',j'}}(R)-\overline{V_0^{v'',j''}}(R)]\times\exp[-\overline{V_0^{v'',j''}}(R)/kT], \tag{9}$$

where $\rho_0=2.686\,763\times10^{-5}$ mol/Å^3 is Loschmidt's number, and $\overline{V_0^{v,j}}(R)$ is the isotropic part of the full potential averaged over the (v,j) vibrational wave function of the hydrogen diatom. The advantages and limitations of the QS method have been discussed in detail in Ref. 49, where it was found that this extremely simple procedure is suprisingly reliable. It was also pointed out there that the modest difference between the results of CC and QS theory calculations for a given potential could be used to calibrate the latter, to make them effectively equivalent to the former.

Following the suggestions of Ref. 49, the discrepancies between the CC and QS pressure shifting coefficients calculated for the TT_3 H_2–Ar potential surface[18] were used to define a temperature-dependent correction function,

$$\delta(T)\equiv\Delta\nu_{\rm CC}^{\rm TT_3}(T)-\Delta\nu_{\rm QS}^{\rm TT_3}(T), \tag{10}$$

where $\Delta\nu_{\rm CC}^{\rm TT_3}(T)$ are the CC results obtained by Green for the TT_3 potential,[48] and $\Delta\nu_{\rm QS}^{\rm TT_3}(T)$ are the corresponding QS results. The fundamental ansatz of our approach is the assumption that this correction function will be transferable, i.e., that it will be approximately the same for similarly realistic potential energy surfaces. This implies that adding this $\delta(T)$ function to the readily calculated QS results for any realistic H_2–Ar potential will provide a good approximation to the exact CC pressure shifting coefficient for that potential surface:

$$\Delta\nu_{\rm CC}(T)\approx\Delta\nu_{\rm QS}(T)+\delta(T). \tag{11}$$

The calculated frequency shifting coefficients used in the present fits to experimental data were obtained in this way.

Second virial coefficients for H_2–Ar mixtures have been measured in the temperature range of 77–325 K.[44,45] At low temperatures the virial coefficients provide information about the ''volume'' of the potential energy well, while at high temperatures they contain information about the position of the repulsive wall. In the present fits second virial coefficients were calculated using the method of Pack,[69] which includes translational and rotational quantum corrections. These calculations were based on use of two-dimensional H_2–Ar potentials which were obtained from the corresponding full potential by averaging over the $(v,j)=(0,0)$ vibrational wave function of hydrogen.

IV. OUTLINE OF THE FITTING PROCEDURE

The XC model provides a realistic three-dimensional starting potential, XC(0), which is based solely on information derived from theory. Moreover, the realistic shapes of its $E_{\rm HL}^{(1)}$ and ΔE_C components means that a great deal of flexibility is introduced by the ability to adjust the $C_n^{(\lambda)}(\xi)$ functions within their uncertainties and to determine the scaling factor F from a fit to experimental data. In the case of H_2–Ar, for which there is an abundance of experimental data, this flexibility can be exploited to obtain a potential energy surface of substantially higher quality than was previously available.

The present work uses an automatic nonlinear least-squares fitting procedure to optimize simultaneously the agreement with $N_{\rm ir}$ infrared transition frequencies (ir), $N_{\rm ps}$ Raman pressure shifting coefficients (ps), and $N_{\rm vir}$ virial coefficients (vir), as well with the N_{ab} theoretical values of $C_n^{(\lambda)}(\xi)$ listed in Table III (ab). The ability of the model to reproduce the N_α known values of property α (α=ir, ps, vir, ab) is characterized by the dimensionless standard deviation $\overline{\sigma_\alpha}$, defined by

$$\overline{\sigma_\alpha^2}=\frac{1}{N_\alpha}\sum_{i=1}^{N_\alpha}[Y_{\alpha,i}^{\rm obs}-Y_{\alpha,i}^{\rm calc}]^2/u_{\alpha,i}^2, \tag{12}$$

where $Y_{\alpha,i}^{\rm obs}$ denotes the known or observed value of the property Y_α, $Y_{\alpha,i}^{\rm calc}$ the calculated value, and $u_{\alpha,i}$ is the uncertainty associated with that datum. In the case of the infrared data, $u_{{\rm ir},i}^2$ is actually replaced by $[u_{{\rm ir},i}^2+0.04\Gamma_i^2]$, in order to take account of the uncertainty in the calculated eigenvalues for metastable levels, which are estimated to be approximately 20% of the predissociation line widths Γ_i.[18,63,70] Thus, the uncertainty associated with each infrared datum also incorporates the uncertainty due to our method of calculation. A $\overline{\sigma_\alpha}$ value greater than unity would indicate that, on average, the calculated values disagree with experiment by $\overline{\sigma_\alpha}$ times the uncertainty in the data, while a value less than unity implies that, on average, the difference between observation and calculation is less than the uncertainty.

The global dimensionless standard deviation minimized by the fit may be written as

$$\begin{aligned}\overline{\sigma^2}&=\left(\frac{N_{\rm ir}}{N_{\rm tot}}\right)\overline{\sigma_{\rm ir}^2}+\left(\frac{N_{\rm ps}}{N_{\rm tot}}\right)\overline{\sigma_{\rm ps}^2}+\left(\frac{N_{\rm vir}}{N_{\rm tot}}\right)\overline{\sigma_{\rm vir}^2}+\left(\frac{N_{ab}}{N_{\rm tot}}\right)\overline{\sigma_{ab}^2},\\&\equiv\left(\frac{N_{\rm exp}}{N_{\rm tot}}\right)\overline{\sigma_{\rm exp}^2}+\left(\frac{N_{ab}}{N_{\rm tot}}\right)\overline{\sigma_{ab}^2},\end{aligned} \tag{13}$$

where $N_{\rm exp}=N_{\rm ir}+N_{\rm ps}+N_{\rm vir}$ is the total number of experimental data and $N_{\rm tot}=N_{\rm exp}+N_{ab}$. This definition of $\overline{\sigma^2}$ in

TABLE IV. Parameters defining the optimized XC(fit) potential, with their 95% confidence limit uncertainties given in parentheses, where the scaling distance expansion parameters of Eq. (4) are: $R_m^{(0)}=6.783\ 754a_0$, $R_m^{(2)}=0.041\ 267a_0$, and $R_m^{(4)}=-0.002\ 328a_0$.

Short-range parameters:			$F_{0,1}=0.094\ 412$ (0.012)	$F_{2,0}=-0.053\ 489$ (0.0084)		$F_{2,1}=-0.120\ 82$ (0.065)
$F_{0,0}=1.069\ 718$ (0.0054)						
Long-range parameters:		$C_n^{\lambda,k}/E_h a_0^n$				
n	λ	$k=0$	$k=1$	$k=2$	$k=3$	$k=4$
6	0	27.600 68 (0.19)	23.217 3 (0.86)	−0.700 9 (2.5)	−4.366 (1.13)	1.057 (2.4)
6	2	2.623 7 (0.029)	5.586 8 (0.13)	2.354 (0.50)	−1.658 6 (0.12)	−1.0495
8	0	602.294 (15)	696.18 (72)	329.40 (152)	−57.1 (80)	−153.8 (144)
8	2	151.54 (9.8)	450.8 (54)	404.9 (206)	95.9 (89)	−9.74
8	4	7.273 (0.84)	27.835 (5.9)	32.42 (19)	8.08 (9.3)	−3.778
10	0	21 858.6 (1120)	36 546. (4970)	29 044 (4 170)	10 708 (4670)	−714 (5280)
10	2	4 796.7 (600)	15 843 (3290)	16 673 (11 900)	6 063 (6220)	436.3
10	4	278.3 (63)	1 055.6 (493)	1 524 (1 540)	2 541 (1850)	1794.3
10	6	27.36	79.74	95.23	122.58	79.73

terms of the component values $\overline{\sigma_\alpha^2}$ was introduced so that the quality of the fit to individual properties may be compared to each other and to the quality of the overall fit in an equivalent manner. Thus, the value of $\overline{\sigma_{\rm exp}}$ provides a measure of the ability of the parametrized potential model to reproduce the overall experimental data set, while the value of $\overline{\sigma_{ab}}$ indicates the degree to which the constraints on the $C_n^{(\lambda)}(\xi)$ are satisfied.

In the optimization of the model, the $C_n^{\lambda,4}$ coefficients for $\lambda>0$ were not varied explicitly, but were constrained by Eq. (7). In addition, the $C_{10}^{6,k}$ coefficients were determined solely from the *ab initio* values of $C_{10}^{(6)}(\xi)$, as the experimental data seemed completely insensitive to their values; the seven nonzero values of $C_{10}^{(6)}(\xi)$ were therefore omitted from the ''*ab*'' data set used in the fits. As a result, 39 parameters were varied simultaneously in a least-squares fit to a set of observations consisting of $N_{\rm exp}=190$ experimental data ($N_{\rm ir}=171$, $N_{\rm ps}=8$, and $N_{\rm vir}=11$) and 59 nonzero $C_n^{(\lambda)}$ values ($N_{ab}=59$; see Table III). The parameters varied explicitly in the fits were therefore:

4 short-range parameters: $F_{0,0}$, $F_{0,1}$, $F_{2,0}$, $F_{2,1}$

35 long-range parameters: $\{C_n^{0,k}|n=6,8,10;\ 0\leqslant k\leqslant 4\}$

$\{C_n^{2,k}|n=6,8,10;\ 0\leqslant k\leqslant 3\}$

$\{C_n^{4,k}|n=8,10;\ 0\leqslant k\leqslant 3\}$.

It is important to realize, however, that the 35 long-range parameters serve primarily to represent the input $C_n^{(\lambda)}(\xi)$ data. In other words, most of the parameters being varied in these fits are not truly ''free'' empirical parameters, since the long-range coefficient expansions are largely determined by the input data of Table III, and most are only slightly modified by the fits to the experimental data. Thus, the fits to experimental data mainly determine the four truly empirical parameters, the $F_{\lambda,k}$ of Eq. (8), with modest, but nevertheless important additional flexibility being introduced by treating the long-range multipolar interaction energy constants (weighted by their uncertainties) like experimental data in the analysis.

The fits to determine the set of potential parameters which minimize $\overline{\sigma^2}$ require values of the partial derivatives of $Y_{\alpha,i}^{\rm calc}$ (for α=ir, ps, and vir) and of $C_n^{(\lambda)}(\xi)$ with respect to the potential parameters. For the experimental data, the derivatives with respect to a potential parameter p_j were calculated by symmetric finite differences,

$$\frac{\partial Y_{\alpha,i}^{\rm calc}}{\partial p_j}\approx\frac{Y_{\alpha,i}^{\rm calc}(p_j+\Delta p_j)-Y_{\alpha,i}^{\rm calc}(p_j-\Delta p_j)}{2\Delta p_j}, \tag{14}$$

whereas the derivatives of the $C_n^{(\lambda)}(\xi)$ were evaluated analytically,

$$\frac{\partial C_n^{(\lambda)}(\xi)}{\partial C_{n'}^{\lambda',k}}=\delta_{n,n'}\delta_{\lambda,\lambda'}\xi^k. \tag{15}$$

These equations show that to calculate the derivatives for a given set of trial parameter values, the experimental data set must be computed $(2N_p+1)$ times, where N_p denotes the number of parameters being varied. Since the experimental data must be computed many times during the optimization, it is imperative to simulate the data using methods which are extremely efficient.

V. OPTIMIZED XC POTENTIAL ENERGY SURFACE FOR H_2–Ar

The optimized XC potential for H_2–Ar determined by our analysis is denoted XC(fit); the values of the $F_{\lambda,k}$ and $C_n^{\lambda,k}$ parameters which define it are listed, with their 95% confidence limit uncertainties (in parentheses), in Table IV. Some of the uncertainty in the optimized parameters of Table IV is due to uncertainty in the data or inadequacies of the fit, but most arises from interparameter correlation, i.e., from the fact that changes in one parameter may be partly compensated for by correlated changes in one or more of the others. With one noteworthy exception (see below), the similarity of the $C_n^{(\lambda)}$ functions for the XC(0) and XC(fit) potentials (see Fig. 1) confirms the assertion that they are largely determined by the theoretical input ''data'' and their uncertainties, and are not truly free parameters in the fits to the experimental data.

The quality of our fit to the individual properties is indicated by the dimensionless standard deviations which are listed in Table V, together with analogous predictions for

TABLE V. Dimensionless root mean square deviation from experiment ($\overline{\sigma_\alpha}$) of predictions of property α yielded by several different H_2–Ar potentials.

	Ref.	# data	Potential			
			XC(fit)	TT_3	SAPT	XC(0)
Properties used in the fit						
(a) IR spectra	37	171	0.78	5.63	21.7	71.0
(b) Pressure shifting coefficients	38, 39	8	1.65	49.0	93.5	40.3
(c) Virial coefficients	40, 41	11	0.78	0.72	1.10	1.22
Sum of (a), (b), and (c), as used in fits		190	0.83	11.8	28.9	67.4
Properties not used in the fit						
Total cross sections for $13.5° \leqslant \theta_{lab} \leqslant 34°$	55, 56	52	0.83	0.88	1.21	1.13
Total cross sections for $34° < \theta_{lab}$	55, 56	17	0.48	0.57	0.54	0.45
Inelastic cross sections	55, 56	3	0.46	0.39	1.98	8.53
Hyperfine transition frequencies	57	5	1.06	0.46	65.7	156.8

certain other potential energy surfaces. They show that the XC(fit) potential reproduces the experimental data and the ξ-dependent long-range interaction energy coefficients very well: $\overline{\sigma_{\rm exp}}=0.83$, while $\overline{\sigma_{ab}}=1.25$ and the overall $\overline{\sigma}=0.95$. The agreement with the spectroscopic data is remarkably good, and is particularly impressive when expressed in absolute terms: the average experimental uncertainty in the IR transition frequencies is estimated[1] to be 0.005 cm^{-1}, and the average difference between the calculated and observed frequencies, which is approximately 0.78×0.005 $cm^{-1}=0.0039$ cm^{-1}, is distinctly less than this average uncertainty. Comparison of the entries in Table V for the XC(0) and XC(fit) potentials indicates that we were able to improve the agreement with the IR data by a factor of almost 100, through the use of a very simple four-parameter representation of the scaling function F [see Eq. (8)] and the flexibility associated with the fit to the $C_n^{(\lambda)}(\xi)$ data. The improvement in the agreement with the pressure shifting coefficients is also substantial, and much of the remaining apparent discrepancy may well reflect overly optimistic estimates of the experimental and computational uncertainties.[42,43] However, the virial coefficients seem only moderately sensitive to the differences among these potentials. More detailed comparisons of the experimental IR data with calculations from this optimized XC(fit) potential energy surface are presented by McKellar.[1]

Figure 1 compares the input values of $C_n^{(\lambda)}(\xi)$ and their estimated uncertainties (from Table III, points, and/or error bars) with the corresponding fitted functions associated with the XC(0) (dashed curves) and XC(fit) (solid curves) potentials. It shows that, with the noteworthy exception of the $C_{10}^{(0)}(\xi)$ function (discussed below), fitting to the experimental data has modest effects on the functions representing the $C_n^{(\lambda)}(\xi)$ behavior, and that the agreement with the input values is generally well within their estimated uncertainties.

The only significant discrepancy between the input and the XC(fit) results seen in Fig. 1 occurs for the isotropic $C_{10}^{(0)}(\xi)$ function, for which the fitted values are systematically larger than the *ab initio* ones. We believe that the marked dependence of this discrepancy on ξ is an artifact of the weights used in the fits, and that the essential point is that the experimental data require the average value of $C_{10}^{(0)}(\xi)$ [$\overline{C_{10}^{(0)}}$, which approximates $C_{10}^{(0)}(\xi=0)$] to be roughly 40% (some 5 times the estimated uncertainty) larger than is implied by the *ab initio* input values. The net effect is that in addition to the four unconstrained scaling function parameters $F_{\lambda,k}$, this adjustment of $\overline{C_{10}^{(0)}}$ effectively introduces a fifth empirically determined parameter into our analysis. This result implies that the present model for ΔE_C does not include sufficient high-order inverse-power behavior, and

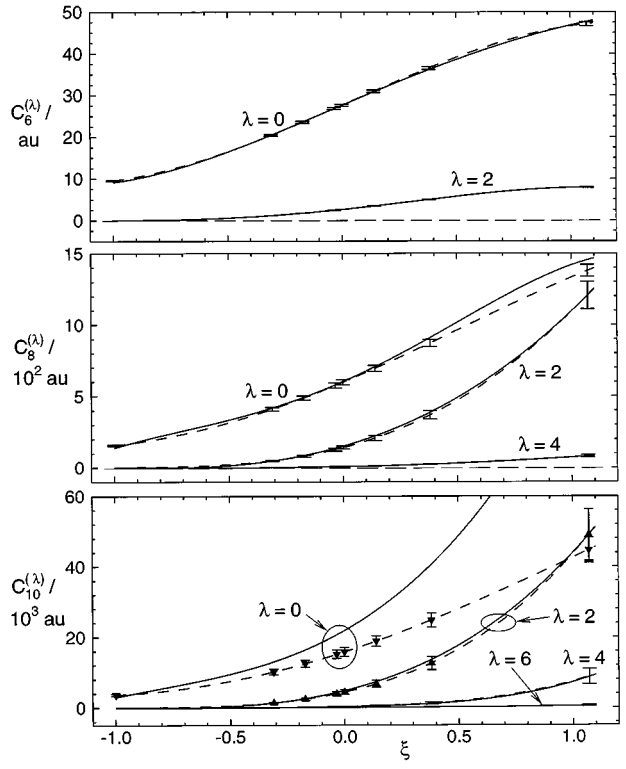

FIG. 1. Long-range stretching-dependent potential energy coefficients $C_n^{(\lambda)}(\xi)$ for H_2–Ar; the input theoretical values (Ref. 57) and their estimated uncertainties are shown as points and/or error bars, while the fitted functions associated with the XC(0) and XC(fit) potentials are shown as dashed and solid curves, respectively.

TABLE VI. Calculated energies (in cm^{-1}) for various levels of $H_2(v,j)$–Ar based on the recommended XC(fit) potential energy surface. For each quasibound level, the predissociation linewidth (in cm^{-1}) is given in brackets below the calculated energy.

		$v=0,\ j=0$	$v=0,\ j=1$			$v=1,\ j=0$	$v=1,\ j=1$		
n	l	$J=l$	$J=l-1$	l	$l+1$	$J=l$	$J=l-1$	l	$l+1$
0	0	−21.952	[a]	[a]	−22.317	−23.014	[a]	[a]	−23.440
	1	−20.832	−22.277	−20.152	−21.205	−21.899	−23.462	−21.162	−22.322
	2	−18.603	−19.003	−17.925	−18.980	−19.681	−20.081	−18.942	−20.103
	3	−15.295	−15.686	−14.619	−15.672	−16.386	−16.791	−15.646	−16.808
	4	−10.952	−11.336	−10.282	−11.327	−12.057	−12.461	−11.318	−12.478
	5	−5.649	−6.023	−4.994	−6.017	−6.760	−7.161	−6.030	−7.176
	6	0.485	0.128	1.105	0.134	−0.610	−0.999	0.094	−1.012
		(0.000)	(0.000)	(0.000)	(0.000)			(0.000)	
	7	7.14	6.83	7.69	6.83	6.13	5.78	6.76	5.77
		(0.22)	(0.18)	(0.33)	(0.18)	(0.09)	(0.08)	(0.17)	(0.07)
1	0	−0.405	[a]	[a]	−0.426	−0.553	[a]	[a]	−0.571
	1	−0.075	−0.185	−0.035	−0.091	−0.179	−0.330	−0.120	−0.202

[a]Because of angular momentum coupling considerations, this level does not exist.

that a better ΔE_C model which includes $C_{12}^{(0)}(\xi)$ terms is needed to give a truly optimum fit to all the data. This is the first clear example in which an XC potential energy model based on a truncation of ΔE_C at terms varying as R^{-10} was unable to adequately represent experimental data.[4,6,71] This is partly due to the high estimated reliability of the input $C_n^{(\lambda)}(\xi)$ values for the H_2–Ar interaction relative to those available (at the time) for other systems to which this approach has been applied.

In order to illustrate the effects of vibrational and centrifugal stretching on some properties of these species, Tables VI and VII list the energies of all bound and quasibound levels of the complexes formed by $j=0$ and 1 H_2 and D_2 in both the $v=0$ and $v=1$ vibrational levels.[72] In addition to the diatom vibrational and rotational quantum numbers v and j, states of the complex are labeled by the quantum numbers n and l for the vibrational stretching and end-over-end rotation of the van der Waals bond **R**, and the total

TABLE VII. Calculated binding energies (in cm^{-1}) for various levels of $D_2(v,j)$–Ar based on the recommended XC(fit) potential energy surface. For each quasibound level, the predissociation linewidth (in cm^{-1}) is given in brackets below the calculated energy.

		$v=0,\ j=0$	$v=0,\ j=1$			$v=1,\ j=0$	$v=1,\ j=1$		
n	l	$J=l$	$J=l-1$	l	$l+1$	$J=l$	$J=l-1$	l	$l+1$
0	0	−28.366	[a]	[a]	−29.103	−29.193	[a]	[a]	−30.015
	1	−27.739	−29.364	−26.942	−28.368	−28.569	−30.296	−27.719	−29.267
	2	−26.487	−26.580	−25.689	−27.062	−27.323	−27.382	−26.472	−27.958
	3	−24.617	−24.819	−23.818	−25.160	−25.461	−25.646	−24.607	−26.059
	4	−22.137	−22.394	−21.336	−22.660	−22.992	−23.243	−22.135	−23.567
	5	−19.060	−19.349	−18.258	−19.569	−19.927	−20.217	−19.068	−20.486
	6	−15.402	−15.711	−14.601	−15.899	−16.283	−16.598	−15.420	−16.830
	7	−11.186	−11.509	−10.389	−11.673	−12.082	−12.413	−11.220	−12.618
	8	−6.443	−6.773	−5.653	−6.919	−7.350	−7.693	−6.494	−7.876
	9	−1.214	−1.548	−0.441	−1.677	−2.130	−2.478	−1.284	−2.642
	10	4.429	4.099	5.172	3.985	3.520	3.172	4.339	3.028
		(0.000)	(0.001)	(0.001)	(0.000)	(0.000)	(0.000)	(0.000)	(0.000)
	11	10.35	10.04	11.03	9.95	9.48	9.14	10.24	9.02
		(0.08)	(0.08)	(0.14)	(0.06)	(0.04)	(0.04)	(0.08)	(0.03)
	12	16.49	16.20	17.16	16.12	15.63	15.31	16.36	15.21
		(0.8)	(0.7)	(1.0)	(0.7)	(0.5)	(0.4)	(0.7)	(0.4)
1	0	−4.379	[a]	[a]	−4.534	−4.745	[a]	[a]	−4.929
	1	−3.989	−4.550	−3.725	−4.137	−4.351	−4.968	−4.059	−4.523
	2	−3.219	−3.354	−2.964	−3.361	−3.572	−3.707	−3.289	−3.735
	3	−2.095	−2.227	−1.855	−2.228	−2.433	−2.571	−2.163	−2.586
	4	−0.665	−0.788	−0.451	−0.784	−0.975	−1.108	−0.730	−1.113
	5	0.95	0.85	1.11	0.87	0.701	0.583	0.894	0.590
		(0.05)	(0.04)	(0.10)	(0.03)	(0.012)	(0.017)	(0.036)	(0.006)
	6					2.55	2.46		2.46
						(0.7)	(0.6)		(0.6)

[a]Because of angular momentum coupling considerations, this level does not exist.

angular momentum quantum number J. Levels with positive energies are ''quasibound'' states which lie above the relevant potential asymptote and can dissociate by tunneling through the associated effective centrifugal potential barrier. Their tunneling predissociation lifetimes can be determined from the level widths which are given in parentheses below each (positive) level energy.[63,70] In accord with the value of the quality of fit parameter $\overline{\sigma_{\rm ir}}$, the level energy spacings are believed to be accurate to within $\sim 0.004\ {\rm cm}^{-1}$, but the uncertainties in their absolute binding energies [calculated using Eq. (30) of Ref. 32] are $\sim 0.02\ {\rm cm}^{-1}$.

The differences between the level energies for complexes formed from the diatom in states $v=0$ and $v=1$ illustrate the effect of the monomer vibrational stretching on the potential surface. Similarly, the difference between the energy of a (v,j,n,l,J) level for $j=0$ and the average over J of the three corresponding $j=1$, $J=l$, $l\pm 1$ levels illustrates the effect of centrifugal stretching of the H_2 or D_2 on the vibrationally averaged potential surfaces and the levels they support. It is also interesting to note that the large zero point energy, of approximately half the well depth, together with the extreme anharmonicity of the potential near its asymptote, mean that the vibrational isotope shifts are quite modest, in spite of the fact that the reduced masses of the two isotopomers differ by a factor of 2. Note too that in addition to differences in the reported energies, these results differ from the SAPT potential predictions of Ref. 73 in that they show that H_2–Ar (as well as D_2–Ar) actually has *two* bound van der Waals stretching states.

It is relevant to also comment on the choice of the functional form used for the XC potential, as summarized by Eqs. (2)–(8), especially in regard to its bond-stretch or ξ dependence. Since each of the components F, $E_{\rm HL}^{(1)}$, and ΔE_C may be written as a linear power series in ξ, the overall potential may be expanded as

$$V(R,\theta,\xi)=\sum_{k=0}^{4}\xi^k U_k(R,\theta). \tag{16}$$

For the homonuclear H_2 isotopomers,[74] the ξ dependence of the potential may then be fully taken into account by simply replacing these powers of ξ^k by appropriate values of the expectation values or matrix elements $\langle v',j'|\xi^k|v'',j''\rangle$ for various hydrogen isotopomers, which are readily available and/or readily calculated.[50] Maintaining this simple linear dependence on matrix elements of powers of ξ is a key reason for *not* allowing the scaling distance R_s [see Eq. (4) and the discussion below Eq. (5)] to be a function of ξ. Note, however, that in spite of the definition of r_0 given below Eq. (2), the two-dimensional vibrationally averaged potential for ground-state H_2 is *not* simply $U_0(R,\theta)$, since expectation values of higher powers of ξ are not zero for $H_2(v=0,j=0)$. Of course the fact that the angle dependence of the potential is built into the Heitler–London exponent and damping function scaling distance $R_s=R_m(\theta,\xi=0)$ means that expanding the $U_k(R,\theta)$ functions in terms of the familiar $V_{\lambda,k}(R)$ functions of Eq. (1) requires the use of numerical quadrature techniques.[74] However, this is true for many other sophisticated potential forms and imposes no significant difficulties.

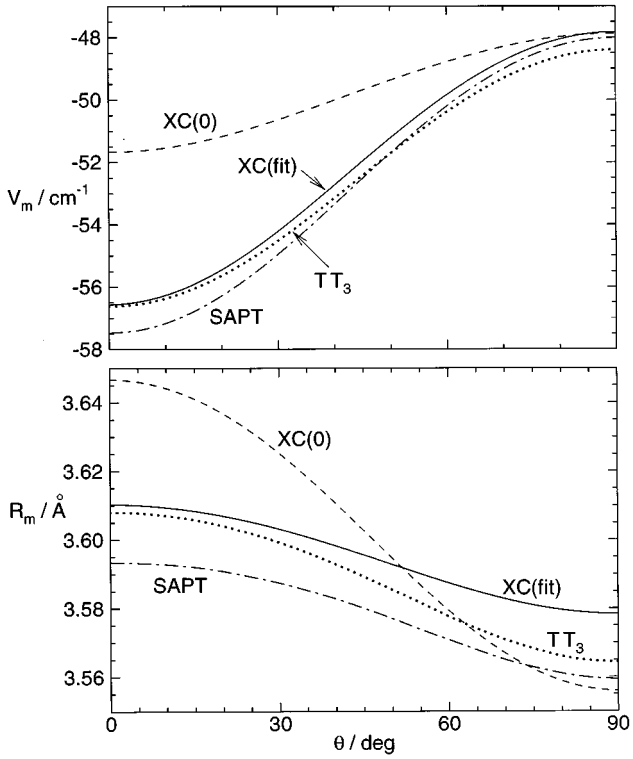

FIG. 2. Variation of the potential minimum (V_m) and its radial position (R_m) with θ (at ξ=0), for four different H_2–Ar potentials.

A FORTRAN subroutine for generating the present recommended XC(fit) potential may be obtained by electronic mail by sending a request to *leroy@theochem.uwaterloo.ca*, or by anonymous *ftp* from directory *pub/leroy/H2Ar* on our computer *theochem.uwaterloo.ca*.[75]

VI. COMPARISON WITH OTHER H_2–Ar POTENTIALS

Detailed calculations have been performed to compare the capabilities of the present recommended XC(fit) potential with other recent high quality potential energy surfaces for H_2–Ar. The other surfaces considered are our *ab initio* based starting potential XC(0), the empirical TT_3 potential of Le Roy and Hutson,[18] and a high quality fully *ab initio* potential obtained using the symmetry-adapted perturbation theory (SAPT) method.[46] The quality of the predictions yielded by these surfaces for a variety of properties are compared in Table V, while the potentials themselves are compared in Figs. 2–4. The present section discusses differences among these potentials and compares the quality of their predictions for the properties used to determine our XC(fit) surface. Section VII will then examine the quality of their predictions for two other classes of experiments which provide independent tests of all four surfaces. Analogous comparisons of the TT_3 potential with earlier surfaces for this system were presented in Ref. 18.

For the four potentials considered here, Fig. 2 shows how the position (R_m) and depth (V_m) of the radial mini-

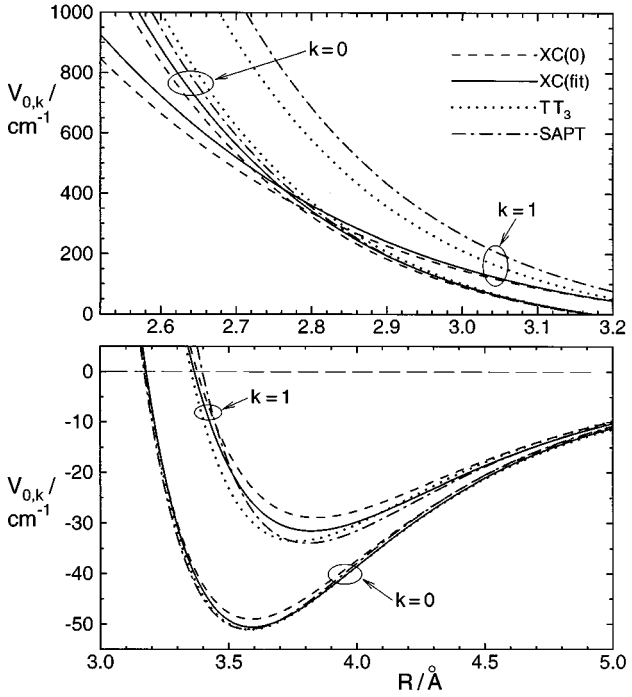

FIG. 3. Radial strength functions $V_{0,0}(R)$ and $V_{0,1}(R)$ of Eq. (1) for four different H_2–Ar potentials.

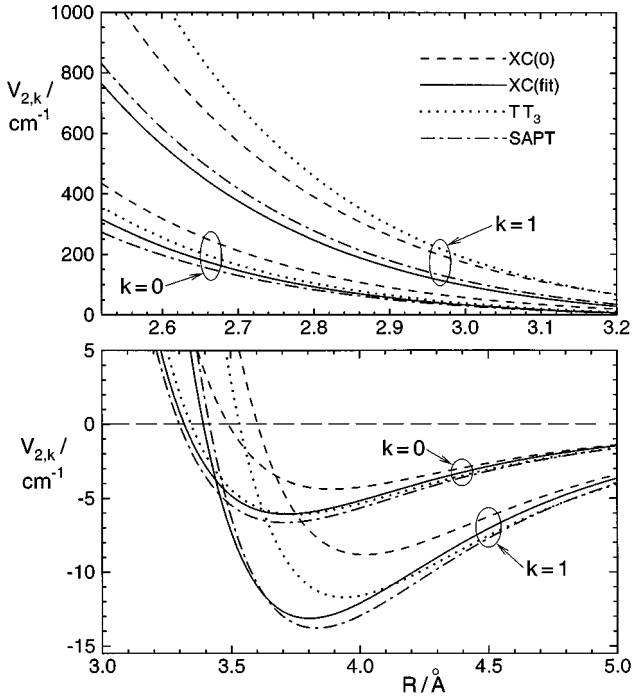

FIG. 4. Radial strength functions $V_{2,0}(R)$ and $V_{2,1}(R)$ of Eq. (1) for four different H_2–Ar potentials.

mum varies with relative orientation, when the H_2 stretching coordinate is fixed at $\xi=0$. For all four cases the global minimum lies at the collinear geometry ($\theta=0$ or π). For the three better surfaces, the well depths vary with angle by approximately 18%, while the corresponding minimum positions vary by only ~1%; for the initial XC(0) surface the corresponding ranges are 8% and 2.6%. Thus, it is clear that the well depth for the XC(0) potential is generally too small and its variation with θ too weak, while its minimum position varies too rapidly with θ. In spite of this marked difference in its anisotropy (see also Fig. 4), it is interesting to note (see Fig. 3) that the isotropic or spherically averaged parts of this potential are quite similar to those of the optimized XC(fit) surface.

Each of the potentials considered here may also be expressed in terms of the double expansion of Eq. (1), and a more conventional way of comparing potentials is in terms of its radial strength functions $V_{\lambda,k}(R)$. For these surfaces, the four leading terms of this expansion are compared in Figs. 3 and 4; Figure 3 shows the basic isotropic potentials $V_{0,0}(R)$ and the coefficients of their linear stretching dependence $V_{0,1}(R)$, while Fig. 4 shows the analogous functions defining the strength of the $P_2(\cos\theta)$ anisotropy, $V_{2,0}(R)$, and its linear stretching dependence, $V_{2,1}(R)$.

It is clear that the basic isotropic potential $V_{0,0}(R)$ is remarkably similar for all four potentials, but there are significant differences among the other components. It is interesting to note that differences among the quality of the predictions of various experimental data may often be correlated with differences or similarities of these radial strength functions. For example, since the second virial coefficients for H_2–Ar are largely determined by the isotropic component of V, it is not surprising that the various calculated values of $\overline{\sigma_{\rm vir}}$ seen in Table V are all similar.

The most accurate previous intermolecular potential for H_2–Ar is the TT_3 surface which Le Roy and Hutson obtained from a least-squares fit to the best then-available IR data and a number of other properties.[18] The fact that its value of $\overline{\sigma_{\rm ir}}=5.6$ is moderately large is not unreasonable in view of the fact that the TT_3 surface was based on fits to a less extensive IR data set whose average uncertainty was four times higher than that for the IR data used here. The size of the $\overline{\sigma_{\rm ir}}$ value for the XC(0) potential ($=71$) reflects the substantial differences between its $k=0$ anisotropy strength function and those of the other potentials in the well region (dashed curves in the lower segment of Fig. 4). Moreover, in view of the differences among the $k=1$ functions seen in Fig. 4, it is perhaps surprising that the TT_3 predictions of the IR data are moderately close to those for XC(fit) and so much better than those of the SAPT potential.

An independent test of the accuracy of the TT_3 potential was provided by Green's close-coupling calculations of Raman Q-branch pressure shifting coefficients for H_2 and D_2 in Ar.[48] The large discrepancies he found (cf. the value $\overline{\sigma_{\rm ps}}=49$ in Table V) were interpreted as showing that the ξ dependence of the isotropic part of the TT_3 potential is not fully reliable in the repulsive wall region. This correlates with the fact that the stretching dependence of the repulsive wall of the isotropic potential (see the dotted curve for $k=1$ in the upper segment of Fig. 3) is distinctly different from that for the XC(fit) potential, for which $\overline{\sigma_{\rm ps}}=1.6$. Similarly, the even larger difference between the $V_{0,1}(R)$ functions for the XC(fit) (solid curves) and SAPT (dot–dashed curves) func-

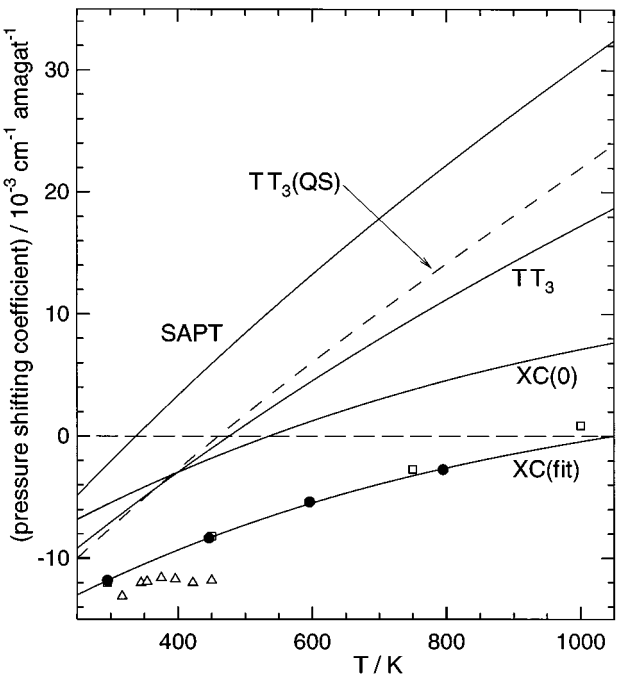

FIG. 5. Pressure shifting coefficients for the Raman $Q_1(0)$ line for H_2 in Ar; the solid circles are the experimental results of Farrow *et al.* (Ref. 42) and the open squares those of Berger *et al.* (Ref. 43). The older experimental results of Lallemand and Simova (Ref. 65) are shown as open triangles, although they were not used in our analysis. The dashed curve represents the raw QS results for the TT_3 potential, while the solid curves are effective CC results generated using Eq. (11).

tions in this region explains the even larger $\overline{\sigma_{ps}}$ value found for the latter. Note that predictions of the starting XC(0) potential are slightly better than those obtained from the TT_3 surface.

A more detailed illustration of the quality of the pressure shifting coefficient predictions for the various potentials is provided by Fig. 5, where the experimental data are shown as points and the ''effective'' close-coupling values yielded by Eq. (11) are shown as solid curves. For the sake of comparison, the dashed curve labeled TT_3(QS) shows the quasistatic theory values for the TT_3 potential obtained directly from Eq. (9). The correction function $\delta(T)$ of Eq. (10) was defined by the difference between points on this dashed curve and Green's[48] CC results for this potential, which effectively define the solid curve labeled TT_3.

It is clear that only the XC(fit) potential reproduces the experimentally measured pressure shifting coefficients. At the same time, it should be pointed out that a preliminary XC(fit) potential based on a fit to only the IR data gave much less accurate predictions of this property, the discrepancies having the opposite sign but approximately the same magnitude as those for the XC(0) potential. Thus, inclusion of the pressure shifting data in the least-squares data set is essential for obtaining an accurate description of the short-range stretching dependence of the isotropic part of the potential, which is the property which governs pure vibrational inelasticity. The similarity between the $V_{0,1}(R)$ functions for the XC(0) and XC(fit) potentials (see Fig. 3) is probably responsible for the fact that the XC(0) function predicts the correct temperature dependence for this property.

VII. INDEPENDENT TESTS OF THE NEW H_2–Ar POTENTIAL

In Sec. VI, the new XC(fit) function and three other potentials were compared with regard to their ability to predict discrete IR spectra, Raman pressure shifting coefficients, and virial coefficients, and Table V shows that the XC(fit) surface provides by far the best overall representation of these data. However, as those data were used in the fits which determined the XC(fit) potential, the good agreement with experiment of its predictions for those properties was not unexpected. In contrast, the present section tests the ability of the four potential surfaces considered above to predict two families of properties which were not used in the above analysis: the elastic and inelastic differential cross sections for D_2 with Ar measured by Buck and co-workers,[59,60] and the hyperfine transitions of H_2–Ar measured by Waaijer and Reuss.[61]

The total differential cross sections are mainly sensitive to the position and shape of the repulsive wall of the isotropic potential up to the experimental collision energy of $\sim$700 cm^{-1}, while the large angle inelastic cross sections depend on the strength of the potential anisotropy in this region.[59] These are features of the potential energy surface which are not directly probed by the experimental data used in the present fits. Moreover, while the short range anisotropy of the TT_3 potential was constrained to give good agreement with the experimental inelastic cross sections, its determination took no account of the total differential cross sections, and of course no experimental data were used in the determination of the XC(0) and SAPT potentials. Thus, these properties provide an objective independent test of the capabilities of these potentials.

As in previous work,[18,60] the total and inelastic differential cross sections were calculated within the coupled states approximation and averaged over the experimental conditions using computer programs kindly supplied by Professor U. Buck. Thus, the calculated elastic and inelastic cross sections presented here are directly comparable with those reported in Refs. 18, 59, and 60. Since those properties effectively depend only on the two-dimensional (R,θ)-dependence of the potential, the full three-dimensional potentials considered here were vibrationally averaged for the ground state of D_2 before being used in these calculations.

For the same four potential energy surfaces considered in Sec. VI, Fig. 6 illustrates the quality of agreement with the experimental total differential cross sections (points) obtained at a collision energy of E_{coll}=83.2 meV. The generally good behavior seen there correlates well with the similarity of the effective isotropic potentials $V_{0,0}(R)$ seen in Fig. 3. As in previous work,[18,60] for more quantitative comparisons the small angle cross sections, sensitive mainly to the position of the low energy repulsive wall, and the large angle region, which depends mainly on the slope of the higher

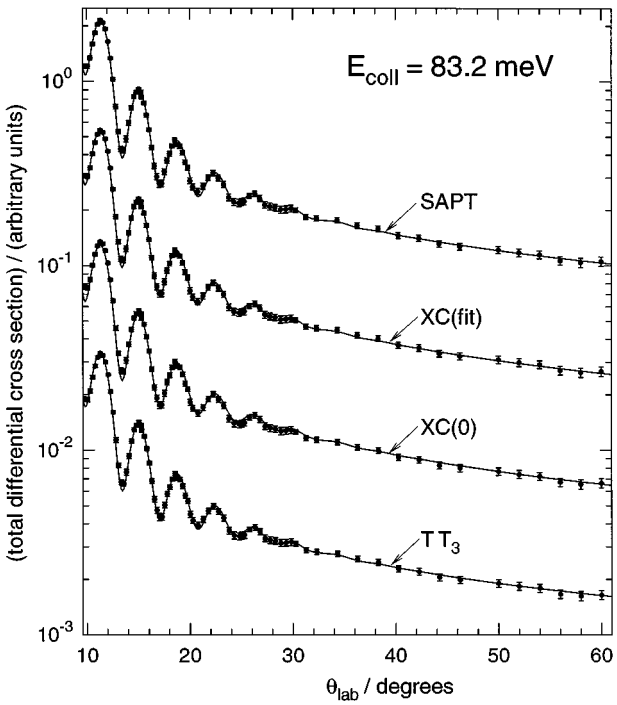

FIG. 6. Comparison with experiment (Refs. 59 and 60, points with error bars, data offset by factors of 4 for the different potentials) of total differential cross sections for D_2 colliding with Ar, calculated from the indicated potential energy surfaces.

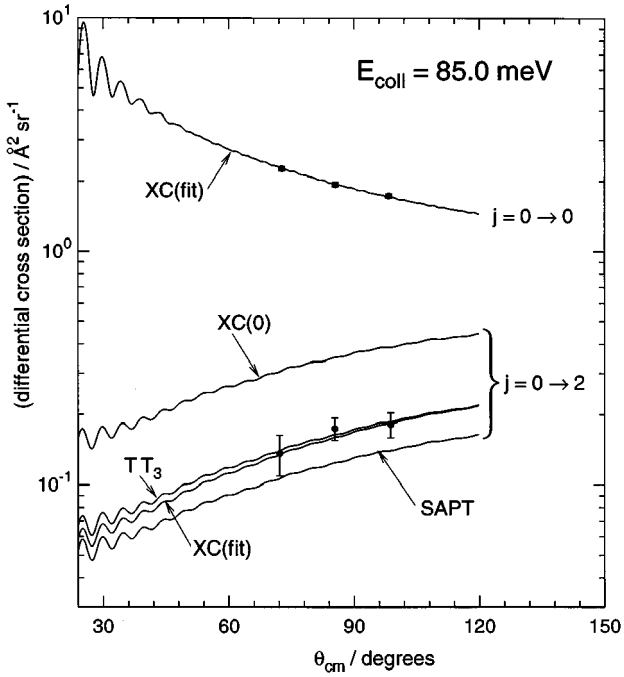

FIG. 7. Comparison with experiment (Refs. 59 and 60, points with error bars) of elastic ($j=0\rightarrow0$) and rotationally inelastic ($j=0\rightarrow2$) cross sections for D_2 colliding with Ar, calculated from the indicated potential energy surfaces.

energy repulsive wall, are considered separately. For these properties, rows 5 and 6 of Table V compare the values of the dimensionless root mean square deviation from experiment yielded by the four potentials under consideration. While all four surfaces appear satisfactory as far as the large angle cross sections are concerned (i.e., their $\overline{\sigma_\alpha}$ values are all <1.0), the small angle data discriminate somewhat against the XC(0) and SAPT surfaces.

For the rotationally inelastic $j=0\rightarrow2$ cross sections for D_2, Fig. 7 and row 7 of Table V illustrate the quality of agreement with experiment yielded by the various potentials. On the scale of Fig. 7, the various predictions for the elastic cross sections are essentially equivalent, but those for the inelastic process are not. Once again, the TT_3 and XC(fit) predictions are in full agreement with experiment ($\overline{\sigma_\alpha}<1.0$), while those of the SAPT and XC(0) potentials lie outside of the experimental uncertainties. It is interesting to note that the fact that the SAPT predictions are slightly too small and the XC(0) predictions distinctly too large correlates with the relative strengths of the short-range anisotropy strength functions $V_{2,0}(R)$ seen in the upper segment of Fig. 4. While the TT_3 surface was constrained to give good agreement with this property,[18] the quality of the agreement for the XC(fit) potential provides a completely independent confirmation of its reliability. Indeed, for both elastic and inelastic cross sections, the predictions of the XC(fit) potential agree with experiment as well as those of the best-fit two-dimensional potential determined[59,60] from a direct fit to those data.

As discussed in Ref. 18, the hyperfine transitions at radio frequencies measured by Waaijer and Reuss[61] depend mainly on the expectation value of the anisotropy strength function for levels of H_2–Ar formed from ground state *ortho* hydrogen ($v=0$, $j=1$). Those measurements were included in the data set which determined the TT_3 potential, so good agreement there was expected; however, they provide an independent test of the other potentials considered here. The results in the last row of Table V show that the present recommended XC(fit) potential predicts these data essentially within the experimental uncertainties, while the SAPT and particularly the XC(0) potential do much worse. The relative quality of these results also correlates well with the degree of similarity of the anisotropy strength functions $V_{2,0}(R)$ in the attractive region, seen in the lower segment of Fig. 4.

VIII. CONCLUSIONS

This paper has presented the construction of a reliable new three-dimensional potential energy surface for the H_2–Ar system, which is based on the XC potential model.[2–6] The results show that the XC model is sufficiently realistic and flexible that only five effectively free empirical parameters are required in the least-squares fits to optimize agreement with high quality experimental data. This contrasts with the eight parameters (plus additional intuitively justified constraints) required to define the best previous potential for this system.[18] The resulting optimized XC(fit) potential provides the most accurate present description of the experimental data for the H_2–Ar interaction, and since it is constructed from realistic theoretical components, it is expected to extrapolate well into regions not directly sampled by the ex-

perimental data used in the analysis. This appears to be confirmed by the quality of its predictions of the differential scattering and hyperfine data. The realistic nature of the components of the basic XC model is an important feature in the determination of potentials for complexes formed with He or Ne, for which the relatively small number of bound states and relatively large zero point energy[76] would introduce a particularly high degree of model dependence into a purely empirical analysis. While the potential form is somewhat complex, its availability as a FORTRAN subroutine (see Sec. V) should obviate difficulties in applying it.

Another noteworthy point is the fact that within the average experimental discrepancy of 0.004 cm^{-1}, the 94 IR transitions for H_2–Ar and 77 for D_2–Ar are fully accounted for by the same three-dimensional potential energy surface. In other words, within this resolution the differences between the IR spectra of these isotopomers are fully accounted for by ordinary mass and vibrational averaging (over ξ) considerations, so that *no Born–Oppenheimer breakdown effects* are evident.

The SAPT method is probably the best fully *ab initio* procedure for calculating van der Waals potentials currently in use.[46,77–79] In view of the fact that no experimental data were used to refine it, the agreement of the SAPT potential of Ref. 46 with the fitted potentials, and the quality of the predictions it yields (see Table V, Figs. 6 and 7, and Ref. 73) are really remarkably good. However, those predictions still disagree significantly with experiment. The present work suggests that its greatest deficiencies are in the isotropic part of the diatom stretching dependence in the short-range region, which are the portions of the potential responsible for rotational and vibrational inelasticity. In any case, it is clear that further developments are necessary before such potentials will truly take the place of empirically refined surfaces such as the present XC(fit) function.

In conclusion, therefore, we believe that the most productive means of developing realistic and flexible multidimensional potential energy surface models for van der Waals interactions is the type of approach used here. The component Heitler–London and Coulomb interaction energies are relatively easy to calculate, and even without adjustment give a reasonable approximation to the final optimized isotropic surface. The fact that they build in very realistic descriptions of the shapes of, and interactions between, the component species also means that relatively few empirical parameters are required to refine such models to yield state-of-the-art potentials.

ACKNOWLEDGMENTS

We are grateful to Professor U. Buck for providing the programs used for simulating the scattering data, and to Professor F. R. W. McCourt and Professor A. J. Thakkar for helpful discussions. Funding for this research was provided by the Natural Sciences and Engineering Research Council of Canada and through the Network of Centres of Excellence in Molecular and Interfacial Dynamics.

[1] A. R. W. McKellar, J. Chem. Phys., preceding paper, **105**, 2628 (1996).
[2] K.-C. Ng, W. J. Meath, and A. R. Allnatt, Chem. Phys. **32**, 175 (1978).
[3] K.-C. Ng, W. J. Meath, and A. R. Allnatt, Chem. Phys. **37**, 237 (1979).
[4] W. J. Meath, D. J. Margoliash, B. L. Jhanwar, A. Koide, and G. D. Zeiss, in *Proceedings of the 14th Jerusalem Symposium on Quantum Chemistry and Biochemistry*, edited by B. Pullman (Reidel, Dordrecht, 1981), pp. 101–115.
[5] R. A. Aziz, M. J. Slaman, A. Koide, A. R. Allnatt, and W. J. Meath, Mol. Phys. **77**, 321 (1992); A. K. Dham, W. J. Meath, A. R. Allnatt, R. A. Aziz, and M. J. Slaman, Chem. Phys. **142**, 173 (1990); A. K. Dham, A. R. Allnatt, W. J. Meath, and R. A. Aziz, Mol. Phys. **67**, 1291 (1989), and references therein.
[6] W. J. Meath and M. Koulis, J. Mol. Struct. **226**, 1 (1991).
[7] R. J. Wheatley and W. J. Meath, Mol. Phys. **79**, 253 (1993).
[8] W. J. Meath, *Atomic Physics and Quantum Optics*, edited by H. A. Bachor, K. Kumar, and B. A. Robson (World Scientific, New York, 1993).
[9] M. Koulis, T. H. Wu, A. K. Dham, R. J. Wheatley, A. R. Allnatt, and W. J. Meath (unpublished).
[10] R. J. Le Roy, C. Bissonnette, T. H. Wu, A. K. Dham, and W. J. Meath, Faraday Discuss. Chem. Soc. **97**, 81 (1994).
[11] A. Dham and W. J. Meath, Chem. Phys. **196**, 125 (1995).
[12] A. K. Dham, F. R. W. McCourt, and W. J. Meath, J. Chem. Phys. **103**, 8477 (1995).
[13] R. J. Le Roy and J. van Kranendonk, J. Chem. Phys. **61**, 4750 (1974).
[14] A. R. W. McKellar and H. L. Welsh, J. Chem. Phys. **55**, 595 (1971).
[15] R. J. Le Roy, J. S. Carley, and J. E. Grabenstetter, Faraday Discuss. Chem. Soc. **62**, 169 (1977).
[16] J. S. Carley, Faraday Discuss. Chem. Soc. **62**, 303 (1977).
[17] R. J. Le Roy and J. S. Carley, Adv. Chem. Phys. **42**, 353 (1980).
[18] R. J. Le Roy and J. M. Hutson, J. Chem. Phys. **86**, 837 (1987).
[19] J. M. Hutson, J. Phys. Chem. **96**, 4237 (1992).
[20] J. M. Hutson, J. Chem. Phys. **96**, 6752 (1992).
[21] R. C. Cohen and R. J. Saykally, J. Chem. Phys. **98**, 6007 (1993).
[22] C. A. Schmuttenmaer, R. C. Cohen, and R. J. Saykally, J. Chem. Phys. **101**, 146 (1994).
[23] M. J. Elrod and R. J. Saykally, J. Chem. Phys. **103**, 933 (1995).
[24] J. Tennyson, Comput. Phys. Rep. **4**, 1 (1986); A. G. Ayllón, J. Santamaría, S. Miller, and J. Tennyson, Mol. Phys. **71**, 1043 (1990).
[25] W. Wang and A. C. Peet, Chem. Phys. Lett. **153**, 98 (1988); A. C. Peet and W. Yang, J. Chem. Phys. **90**, 1746 (1989); **91**, 6598 (1989); R. C. Cohen and R. J. Saykally, J. Phys. Chem. **94**, 7991 (1990).
[26] Z. Bačic and J. C. Light, J. Chem. Phys. **85**, 4594 (1986); J. C. Light and Z. Bačic, *ibid.* **87**, 4008 (1987); Z. Bačic and J. C. Light, Annu. Rev. Phys. Chem. **40**, 469 (1989); S. E. Choi and J. C. Light, J. Chem. Phys. **92**, 2129 (1990).
[27] T. Slee and R. J. Le Roy, J. Chem. Phys. **99**, 360 (1993).
[28] M. J. Bramley and T. Carrington Jr., J. Chem. Phys. **99**, 8519 (1993); M. J. Bramley, J. W. Tromp, T. Carrington Jr., and G. C. Corey, *ibid*. **100**, 6175 (1994); M. J. Bramley and T. Carrington Jr., *ibid*. **101**, 8494 (1994); M. J. Bramley, I. Hamilton, and G. C. Corey, *ibid*. **103**, 9705 (1995).
[29] R. A. Friesner, J. A. Bentley, M. Menou, and C. Leforestier, J. Chem. Phys. **99**, 324 (1993).
[30] C. Leforestier, J. Chem. Phys. **101**, 7357 (1994).
[31] R. T Pack, Chem. Phys. Lett. **55**, 197 (1978).
[32] C. E. Chuaqui, R. J. Le Roy, and A. R. W. McKellar, J. Chem. Phys. **101**, 39 (1994).
[33] A. K. Dham and W. J. Meath, Mol. Phys. **88**, 339 (1996).
[34] M. Thachuk, C. E. Chuaqui, and R. J. Le Roy, J. Chem. Phys. (submitted).
[35] J. Hepburn, G. Scoles, and R. Penco, Chem. Phys. Lett. **36**, 451 (1975); R. Ahlrichs, R. Penco, and G. Scoles, Chem. Phys. **19**, 119 (1977); C. Douketis, G. Scoles, S. Marchetti, M. Zen, and A. J. Thakkar, J. Chem. Phys. **76**, 3057 (1978).
[36] K. T. Tang and J. P. Toennies, J. Chem. Phys. **66**, 1496 (1977); **80**, 3726 (1984).
[37] W. R. Rodwell and G. Scoles, J. Phys. Chem. **86**, 1053 (1982).
[38] R. R. Fuchs, F. R. W. McCourt, A. J. Thakkar, F. B. Van Duijneveldt, and T. van Dam, Mol. Phys. **61**, 109 (1987).
[39] M. S. Bowers, K. T. Tang, and J. P. Toennies, J. Chem. Phys. **88**, 5465 (1988).
[40] R. A. Aziz, in *Inert Gases—Potentials, Dynamics and Energy Transfer in Doped Crystals*, edited by M. L. Klein, Springer Series in Chemical Physics Vol. 34 (Springer, Berlin, 1984), pp. 5–86.

[41] R. A. Aziz and M. J. Slaman, J. Chem. Phys. **92**, 1030 (1990); R. A. Aziz, *ibid*. **99**, 4518 (1993), and references therein.
[42] R. L. Farrow, L. A. Rahn, G. O. Sitz, and G. J. Rosasco, Phys. Rev. Lett. **63**, 746 (1989).
[43] J. Ph. Berger, R. Saint-Loup, H. Berger, J. Bonamy, and D. Robert, Phys. Rev. A **49**, 3396 (1994).
[44] J. Brewer and G. W. Vaughn, J. Chem. Phys. **50**, 2960 (1969).
[45] B. Schramm, E. Elias, and R. Pilger, Chem. Phys. Lett. **88**, 459 (1982).
[46] H. L. Williams, K. Szalewicz, B. Jeziorski, R. Moszynski, and S. Rybak, J. Chem. Phys. **98**, 1279 (1993).
[47] C. Lemaire, R. L. Armstrong, and F. R. W. McCourt, J. Chem. Phys. **87**, 6499 (1987).
[48] S. Green, J. Chem. Phys. **93**, 1496 (1990).
[49] C. E. Chuaqui, Ph.D. thesis, Department of Chemistry, University of Waterloo, 1994.
[50] (a) C. Schwartz and R. J. Le Roy, J. Mol. Spectrosc. **121**, 420 (1987); (b) R. J. Le Roy and C. Schwartz, University of Waterloo Chemical Physics Report No. CP-301R, 1987.
[51] H. Kreek and W. J. Meath, J. Chem. Phys. **50**, 2289 (1969).
[52] A. Koide, W. J. Meath, and A. R. Allnatt, Chem. Phys. **58**, 105 (1981).
[53] R. D. Amos and J. E. Rice, CADPAC—the Cambridge Analytic Derivatives Package, Issue 4.0 (1987).
[54] I. C. Hayes and A. J. Stone, Mol. Phys. **53**, 69 (1984).
[55] B. H. Wells, Mol. Phys. **61**, 1283 (1987).
[56] For convenience, the representation presented in Table I is based on the $R_m(\theta,\xi=0)$ function for our final recommended XC(fit) potential, but an essentially equivalent representation of the $E_{\rm HL}^{(1)}$ data is obtained with other reasonable definitions of R_s. The standard error of the $R_m(\theta,\xi=0)$ fit is $0.5\times10^{-4}a_0$.
[57] P. E. S. Wormer, H. Hettema, and A. J. Thakkar, J. Chem. Phys. **98**, 7140 (1993).
[58] W. J. Meath and A. Kumar, Int. J. Quantum Chem. **24**, 501 (1990).
[59] U. Buck, Faraday Discuss. Chem. Soc. **73**, 187 (1982).
[60] U. Buck, H. Meyer, and R. J. Le Roy, J. Chem. Phys. **80**, 5589 (1984).
[61] M. Waaijer and J. Reuss, Chem. Phys. **63**, 263 (1981).
[62] A. R. W. McKellar, Faraday Discuss. Chem. Soc. (London) **73**, 89 (1982).
[63] J. M. Hutson and R. J. Le Roy, J. Chem. Phys. **83**, 1197 (1985).
[64] I. Mills, T. Cvitaš, K. Homann, N. Kallay, and K. Kuchitsu, *Quantities, Units and Symbols in Physical Chemistry*, 2nd ed. (Blackwell Scientific, Oxford, 1993).
[65] P. Lallemand and P. Simova, J. Mol. Spectrosc. **26**, 262 (1968).
[66] R. Blackmore, S. Green, and L. Monchick, J. Chem. Phys. **88**, 4113 (1988).
[67] S. Green, in *Status and Future Developments in Transport Properties*, edited by W. A. Wakeham (Kluwer Academic, Dordrecht, 1992), p. 257.
[68] S. Green, J. Chem. Phys. **92**, 4679 (1990).
[69] R. T Pack, J. Chem. Phys. **78**, 7217 (1983).
[70] R. J. Le Roy and W.-K. Liu, J. Chem. Phys. **69**, 3622 (1978).
[71] R. A. Aziz, W. J. Meath, and A. R. Allnatt, Chem. Phys. **78**, 295 (1983).
[72] We did not undertake an exhaustive search for quasibound levels lying extremely close to potential barrier maxima, and a limited number having widths >1 cm^{-1} are omitted.
[73] R. Moszynski, B. Jeziorski, P. E. S. Wormer, and A. van der Avoird, Chem. Phys. Lett. **221**, 161 (1994).
[74] W.-K. Liu, J. E. Grabenstetter, R. J. Le Roy, and F. R. McCourt, J. Chem. Phys. **68**, 5028 (1978).
[75] To obtain this material by anonymous *ftp*, begin by using the command *ftp theochem. uwaterloo.cc* to connect to our computer. The response to the userid prompt should be *anonymous* and that to the password prompt should be the caller's e-mail address. The specified subdirectory may then be accessed with the command *cd pub/leroy/subdirectory-name*, and the desired files copied with the command *get filename*.
[76] K. Crowell, C. Bissonnette, R. J. Le Roy, R. J. Wheatley, T. H. Wu, W. J. Meath, and A. R. W. McKellar (unpublished).
[77] B. Jeziorski, R. Moszynski, and K. Szalewicz, Chem. Rev. **94**, 1887 (1994).
[78] R. Moszynski, P. E. S. Wormer, B. Jeziorski, and A. van der Avoird, J. Chem. Phys. **101**, 2811 (1994).
[79] R. Moszynski, T. Korona, P. E. S. Wormer, and A. van der Avoird, J. Chem. Phys. **103**, 321 (1995).
[80] J. M. Standard and P. R. Certain, J. Chem. Phys. **83**, 3002 (1985).